Stationary Features at the Cloud Top of Venus Observed by Ultraviolet Imager Onboard Akatsuki

Kitahara, Takehiko ; Imamura, Takeshi ; Sato, Takao M. ; Yamazaki, Atsushi ; Lee, Yeon Joo ; Yamada, Manabu ; Watanabe, Shigeto ; Taguchi…

(Citation)
Journal of Geophysical Research: Planets,124(5):1266-1281

(Issue Date)
2019-05

(Resource Type)
journal article

(Version)
Version of Record

(URL)
https://hdl.handle.net/20.500.14094/90007271

JGR Planets

RESEARCH ARTICLE
10.1029/2018JE005842

Stationary Features at the Cloud Top of Venus Observed by Ultraviolet Imager Onboard Akatsuki

Takehiko Kitahara[1], Takeshi Imamura[2], Takao M. Sato[3,4], Atsushi Yamazaki[4], Yeon Joo Lee[2], Manabu Yamada[5], Shigeto Watanabe[3], Makoto Taguchi[6], Tetsuya Fukuhara[6], Toru Kouyama[7], Shin-ya Murakami[4], George L. Hashimoto[8], Kazunori Ogohara[9], Hiroki Kashimura[10], Takeshi Horinouchi[11], and Masahiro Takagi[12]

[1]Department of Earth and Planetary Science, The University of Tokyo, Tokyo, Japan, [2]Graduate School of Frontier Sciences, The University of Tokyo, Kashiwa, Chiba, Japan, [3]Space Information Center, Hokkaido Information University, Ebetsu, Hokkaido, Japan, [4]Institute of Space and Astronautical Science, Japan Aerospace Exploration Agency, Sagamihara, Kanagawa, Japan, [5]Planetary Exploration Research Center (PERC), Chiba Institute of Technology, Narashino, Chiba, Japan, [6]College of Science, Rikkyo University, Tokyo, Japan, [7]Artificial Intelligence Research Center, National Institute of Advanced Industrial Science and Technology, Tokyo, Japan, [8]Department of Earth Science, Okayama University, Okayama, Japan, [9]School of Engineering, University of Shiga Prefecture, Hikone, Shiga, Japan, [10]Department of Planetology/Center for Planetary Science, Kobe University, Kobe, Hyogo, Japan, [11]Faculty of Environmental Earth Science, Hokkaido University, Sapporo, Hokkaido, Japan, [12]Faculty of Science, Kyoto Sangyo University, Kyoto, Japan

Key Points:
- Stationary features were observed at the cloud top of Venus in the ultraviolet and attributed to topographic gravity waves
- The features appear above highlands and between noon and the evening
- The scale height of SO_2 was constrained based on modeling of the observed features

Supporting Information:
- Supporting Information S1
- Movie S1

Correspondence to:
T. Imamura,
t_imamura@edu.k.u-tokyo.ac.jp

Citation:
Kitahara, T., Imamura, T., Sato, T. M., Yamazaki, A., Lee, Y. J., Yamada, M., et al. (2019). Stationary features at the cloud top of Venus observed by Ultraviolet Imager onboard Akatsuki. *Journal of Geophysical Research: Planets*, *124*, 1266–1281. https://doi.org/10.1029/2018JE005842

Received 1 OCT 2018
Accepted 12 APR 2019
Accepted article online 23 APR 2019
Published online 15 MAY 2019

Abstract Stationary features indicative of topographic gravity waves were identified at the cloud top of Venus with the 283-nm channel of the Ultraviolet Imager (UVI) onboard Akatsuki, and their geographical and local time dependences were studied. At this wavelength the absorption by SO_2 dominates. To extract stationary structures with respect to the surface, we averaged multiple images to smooth out moving features and applied high-pass filtering to emphasize small structures. We found that stationary features appear exclusively above highlands and that they tend to appear between noon and evening. The stationary features seem to be synchronized with those observed in the cloud top temperature maps taken by the Longwave Infrared Camera (LIR). It was shown using a gravity wave model that the scale height of SO_2 should be smaller than that of the cloud around the cloud top to reproduce the observed phase relationship between the stationary features seen in the Ultraviolet Imager and Longwave Infrared Camera images.

Plain Language Summary Topographic gravity waves, which are atmospheric waves created by winds flowing over mountains, are found to be ubiquitous in the Venus atmosphere. These waves are expected to play crucial roles in the momentum balance of the global-scale atmospheric circulation. The spatial and temporal variabilities of such waves were studied using 283-nm images taken by an ultraviolet camera onboard the Venus orbiter Akatsuki. To extract cloud structures related to topographic gravity waves that are stationary with respect to the surface, multiple images were averaged to smooth out moving features. Topographic waves were found to appear above highlands from noon to evening. The vertical distribution of SO_2, which is the main absorber at this wavelength, around the cloud top was constrained from the observed wave features based on the modeling of wave-induced transport.

1. Introduction

Venus has a cloud layer of sulfuric acid at altitudes of approximately 50–70 km (Mills et al., 2007), where the atmosphere rotates westward up to ~60 times faster than the surface (Schubert et al., 1980). This zonal wind, called the superrotation, diminishes with altitude above the clouds, probably due to the deceleration caused by momentum transport by atmospheric waves (Sánchez-Lavega et al., 2017). However, observational clues about the process have been limited. Here, we focus on stationary atmospheric features related to topographic gravity waves, which are generated by near-surface flows impinging on mountains and propagating upward. Since these waves possess momentum in the direction opposite to the superrotation, their dissipation at high altitudes exerts deceleration on the mean flow.

JAXA's Venus orbiter Akatsuki was inserted into orbit around Venus in 7 December 2015 to explore atmospheric dynamics (Nakamura et al., 2016). In the images taken immediately after the Venus orbit insertion, huge bow-shaped structures extending from northern to southern high latitudes were

discovered by the Longwave Infrared Camera (LIR; Fukuhara et al., 2011) and Ultraviolet Imager (UVI; Yamazaki et al., 2018) onboard Akatsuki, and they continued to exist for more than four Earth days at the cloud top (Fukuhara, Futaguchi, et al., 2017). Similar features have been observed several times by LIR (Kouyama et al., 2017). Since they appear above certain highlands and are always present there, they can be attributed to topographic gravity waves. Fukuhara, Futaguchi, et al. (2017) demonstrated, using a numerical simulation, that bow-shaped structures similar to the observation can be created at the cloud top level by gravity waves. Navarro et al. (2018) reproduced bow-shaped stationary features in a Venusian general circulation model using a subgrid-scale orographic parameterization.

Oscillations of the vertical wind that are attributed to topographic gravity waves have been observed by the VEGA balloons over Aphrodite Terra, which has a top altitude of 3–4 km (Blamont et al., 1986). Recently, Bertaux et al. (2016) suggested, based on cloud tracking using cloud images taken by the Venus Monitoring Camera onboard Venus Express, that the zonal wind speed decreases above Aphrodite Terra, probably due to momentum deposition by topographic gravity waves, although the result of cloud tracking using Akatsuki UVI data does not support this result (Horinouchi et al., 2018). A large number of small structures that are considered to be manifestations of topographic gravity waves were also found in the thermal maps of the cloud top on the nightside by the Visible and InfraRed Thermal Imaging Spectrometer onboard Venus Express (Peralta et al., 2017). Piccialli et al. (2014) studied close-up Venus Monitoring Camera images in the northern high latitude and found that small-scale wavelike features mostly occur above highlands, although it was not confirmed that those features are stationary.

The characteristics of Venusian topographic gravity waves and the mechanism for creating wavelike features at the cloud top are still unclear. In this study, we identify stationary features in UVI images and study their geographical and local time dependences. LIR can map the cloud top temperature, whereas UVI visualizes the distribution of ultraviolet absorbing material. Though UVI can observe the dayside only, unlike LIR that can observe all local time regions, it has the advantage of being able to capture stationary features from longer distances because of its higher resolution. We further model the response of the cloud top atmosphere to gravity waves in order to understand the relationship between the wave features in UVI and LIR images and constrain the altitude distribution of cloud particles and the ultraviolet absorbers in the background atmosphere. Section 2 describes the data set, section 3 gives the analysis procedure and the results, section 4 gives an interpretation using a model, and section 5 gives conclusions.

2. Data Set

The orbit of Akatsuki is elliptical with a revolution period of ~10.5 Earth days, a periapsis altitude of 1,000–8,000 km and an apoapsis altitude of ~360,000 km (Nakamura et al., 2016). UVI takes images of Venus at two wavelengths, 283 and 365 nm, from this elongated orbit. The 283-nm channel corresponds to the absorption band of SO_2, which is abundant below the clouds and decreases rapidly above them (Bertaux et al., 1996; Esposito, 1980; Esposito et al., 1979; Vandaele et al., 2017) because of photochemical conversion to H_2SO_4 clouds (Mills et al., 2007). The 365-nm channel has been used for imaging observations of Venusian clouds for many years, and various species such as Cl_2, $FeCl_3$, S_2O_2, and elementary sulfur are listed as candidates for the absorber, although it has not been identified yet (Mills et al., 2007). This absorber is considered to exist mostly below the cloud top (Esposito, 1980). UVI captures solar radiation scattered by cloud particles, and thus, the observable area is limited to the dayside. The field of view is 12° × 12°, and the number of pixels is 1,024 × 1,024. The pixel resolution varies with the distance to Venus, which is ~200 m at periapsis and ~76 km at apoapsis. More details on UVI are given in Yamazaki et al. (2018).

LIR data are also used for comparison in this study. LIR maps the brightness temperature of the cloud top in the wavelength band 8–12 μm, both on the dayside and nightside. The field of view is 16.4° × 12.4°, and the number of pixels is 328 × 248. The pixel resolution is ~1 km at periapsis and ~300 km at apoapsis. Details on the LIR are given in Fukuhara et al. (2011) and Fukuhara, Taguchi, et al. (2017).

The data product we use is level 3 (L3), in which images were projected onto the longitude-latitude coordinates with a grid interval of 0.125° (Ogohara et al., 2017). The periods of the data analyzed are 7–11 December 2015 and March 2016 to January 2017, spanning more than one Venus year, or 224.7 Earth days. Pairs of UVI images at 283- and 365-nm wavelengths were usually obtained every 2 hr when the spacecraft is not communicating with the tracking station in Japan.

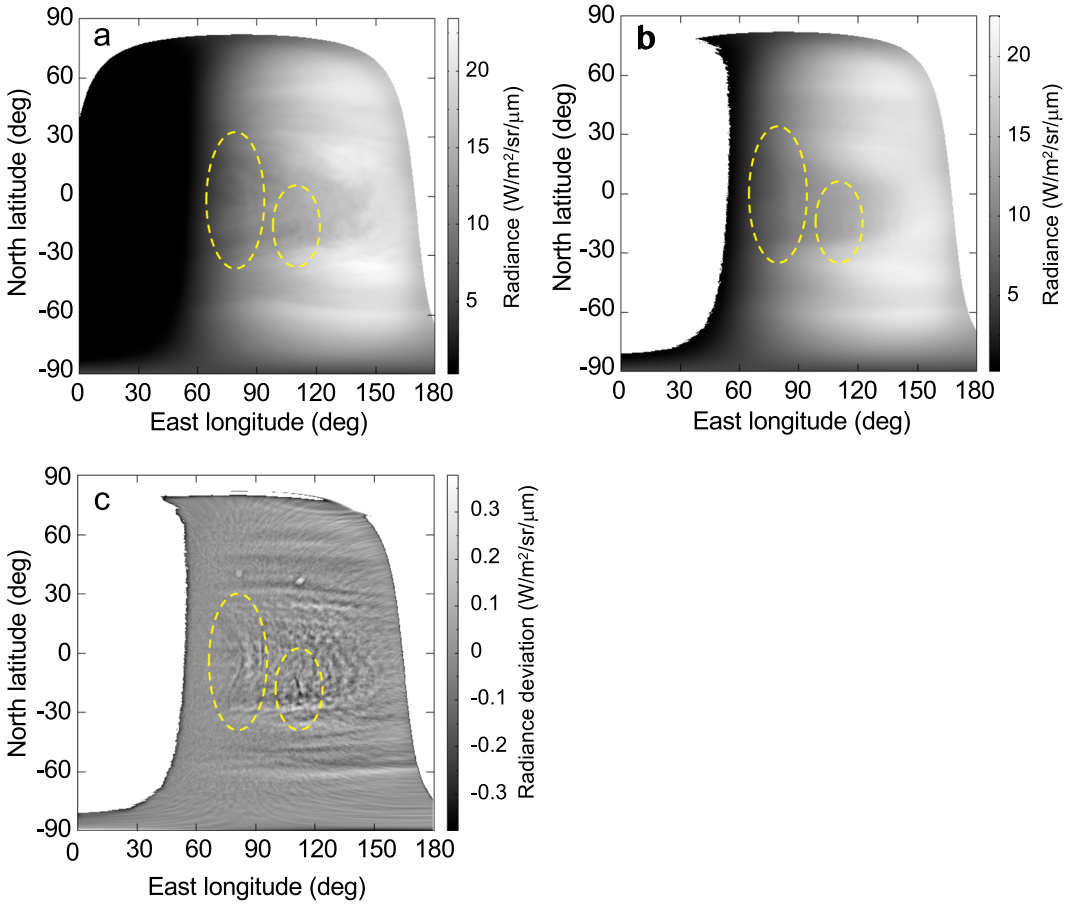

Figure 1. (a) Map projection of a 283-nm image taken at 17:26 on 7 December 2015. (b) Average of five images taken within 9 hr. (c) High-pass filtered map after averaging, with a 3° full width at half maximum Gaussian filter. The locations of stationary features are indicated by ovals.

3. Characteristics of Stationary Features

3.1. Identifying Stationary Features

Figure 1 shows, as an example, the procedure for processing the images taken at the wavelength of 283 nm on 7 December 2015, when LIR also captured the bow-shaped structure for the first time (Fukuhara, Futaguchi, et al., 2017). In the ultraviolet, bow-shaped structures are thought to appear due to the vertical transport of ultraviolet-absorbing substances by gravity waves. Since nonuniform distributions of the absorber due to other processes exist and fluctuate, it is difficult to identify the target structure buried in the background in an unprocessed image (Figure 1a). Therefore, in order to extract structures fixed to the surface, we averaged multiple images taken continuously to smooth out moving features (Figure 1b). The numbers of images averaged in producing the figures shown in this paper are summarized in Table A1. Then, high-pass filtering was applied to the averaged images by subtracting a Gaussian-smoothed image to emphasize small-scale structures (Figure 1c). The full width at half maximum (FWHM) of the Gaussian function is 3°, which corresponds to ~300 km near the equator. Periodic small-scale mottled patterns with a longitudinal interval of ~7° appear because cloud morphology embedded in the superrotating background atmosphere was sampled with a time interval of ~2 hr and remains after the high-pass filtering: 7° in longitude corresponds to 740 km, which is the distance a 100 m/s flow travels in ~2 hr.

In Figure 1c, small-scale bow-shaped structures are identified at longitudes of ~82°E, 93°E, and 110°E near the equator. This region corresponds to Aphrodite Terra (75–140°E, 15°S–5°N). Figure 2a shows an enlarged image of this area with contours of the surface topography, and Figure 2b shows the 365-nm counterpart. The bow-shaped structures indicated by circles in the 283-nm image are almost stationary in movies before averaging (see the supporting information). Unlike the 283-nm image, bow-shaped structures are not clearly

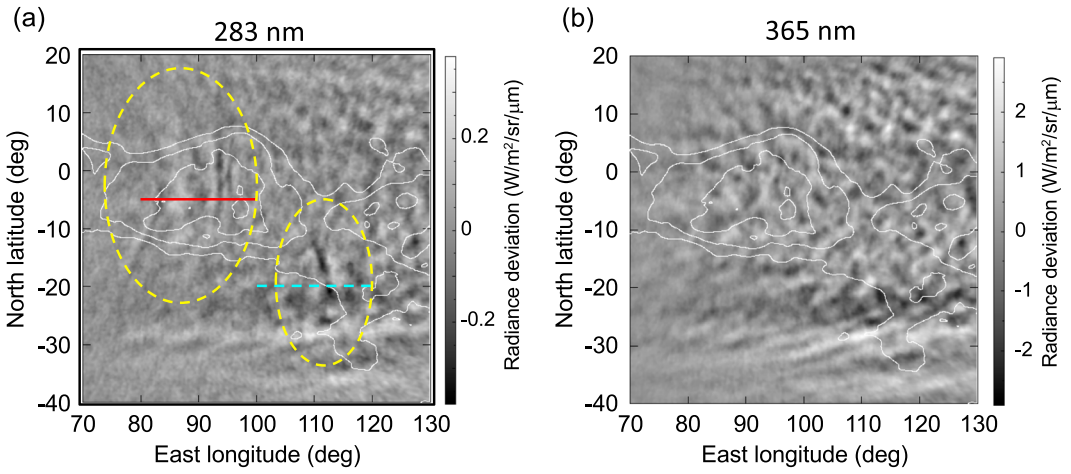

Figure 2. (a) Enlargement of Figure 1c for the wavelength of 283 nm, focusing on Aphrodite Terra, and (b) the 365-nm counterpart. The full width at half maximum of the Gaussian filter is 3°. Average of five images. The locations of stationary features are indicated by ovals. White contours indicate altitudes with 1-km interval for altitudes higher than the global average corresponding to the radius of 6,052 km. The topography data are taken from the Magellan global topography data records in the Planetary Data System of NASA (https://pds.nasa.gov). The red solid line and the light blue dashed line indicate the positions from which the zonal cross-sections in Figure 3 were extracted.

observed in the 365-nm image; this is true of most of the 365-nm images. Figure 3 shows zonal cross-sections of the 283-nm radiance near the center of each structure in Figure 2a extracted from the images taken every ~2 hr without averaging. Stationary peaks and dips indicated by vertical red lines exist at longitudes 83–94°E in the latitude cross-section at 5°S and at longitudes 110–115°E in the latitude cross-section at 20°S.

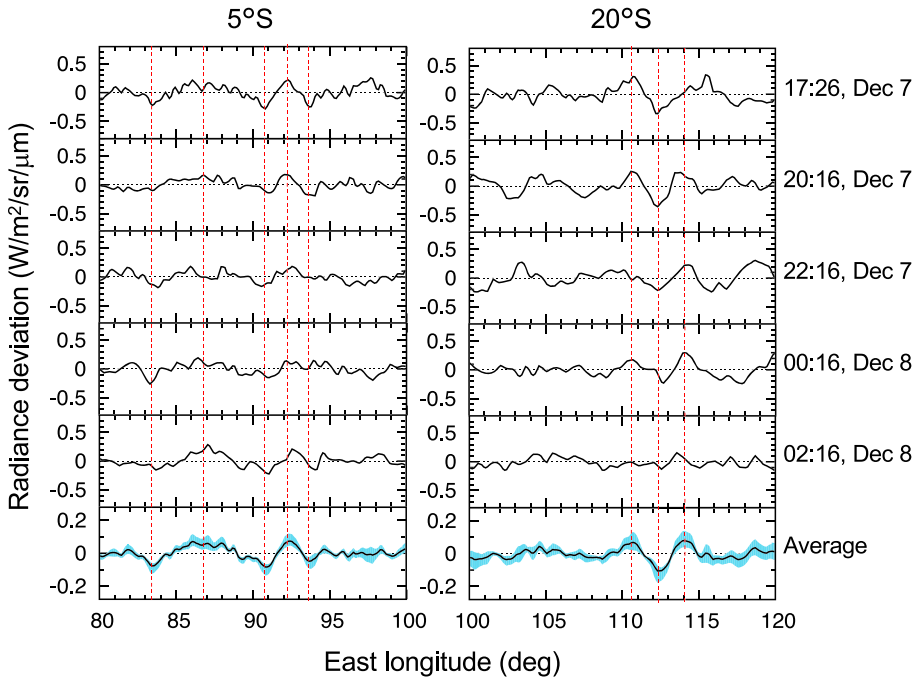

Figure 3. Zonal cross-sections of the high-pass filtered radiance across the bow-shaped structures at 5°S (red line in Figure 2a) and 20°S (yellow line in Figure 2a) seen in the 283-nm images taken on 7 December 2015. The cross-sections before and after averaging are shown. The blue range shows the standard deviation divided by the square root of the number of samples. The time of each image is shown on the right. Red, dashed vertical lines indicate the positions of stationary features.

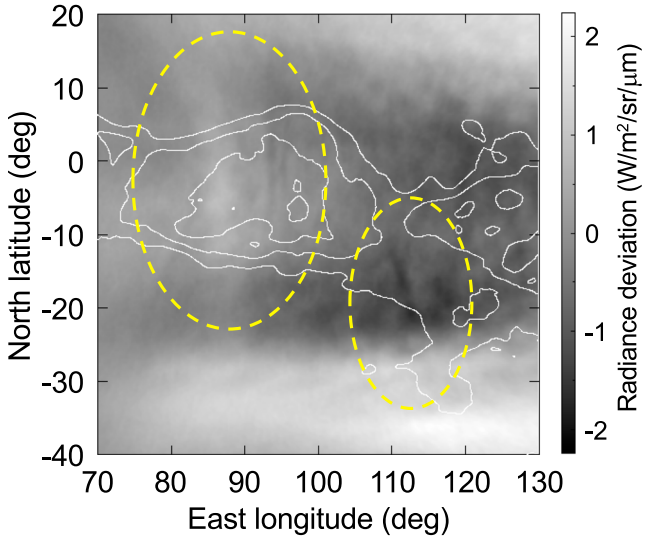

Figure 4. High-pass filtered map after averaging five images at 283-nm wavelength taken on 7 December 2015 focusing on Aphrodite Terran. The full width at half maximum of the Gaussian filter is 30°. The locations of stationary features are indicated by ovals.

A large bow-shaped structure corresponding to the one observed by LIR on 7 December 2015 is only partly seen around 80–90°E in Figure 2. This is because the amplitude of this feature was suppressed by high-pass filtering. With a 30°-FWHM Gaussian filter, the large bow shape becomes more discernible (Figure 4). However, with FWHM values larger than 5°, it is difficult to distinguish small-scale stationary features from background fluctuations in most cases. Therefore, in order to search for small-scale stationary features, the FWHM of the Gaussian filter was set to 3°.

In the 283-nm images analyzed, we detected eight events of stationary features, which are shown in Figure 5. Stationary features tend to appear over highlands in the low and middle latitudes. Although Maxwell Mons in the northern high latitude is the highest (~11 km), no stationary features were found there. All of the stationary features show streaky structures extending in the north-south direction and tend to show wavelike patterns of up to one cycle in the east-west direction. This feature is similar to the ones observed by LIR (Kouyama et al., 2017) and seen in the model result shown in Fukuhara, Futaguchi, et al. (2017). The zonal span of the stationary features is 300–500 km, while the meridional span is up to 2,000–3,000 km, beyond which the bow-shaped structures are difficult to separate from background fluctuations.

Figure 6 shows the locations, the orbits, and the local times where the stationary features were identified. The letters for the locations follow Kouyama et al. (2017), although location B is slightly shifted southward. It is apparent that stationary features tend to appear between noon and evening. This tendency is similar to that of the stationary features seen in LIR images (Kouyama et al., 2017), although the tendency on the nightside is unknown in UVI data; LIR hardly detected stationary features on the nightside.

The stationary feature that appeared on January 2017 above Beta Regio (275–290°E, 20–40°N) was continuously observed over 20 Earth days (Figure 7). The feature gradually emerged in ~3 Earth days, remained visible for ~20 Earth days, and became invisible as it moved to the nightside due to the rotation of Venus. While Kouyama et al. (2017) reported that the stationary feature that appeared on July–August 2016 was not strictly stationary but slowly moved upstream by ~20° in 1 month, the stationary feature shown in Figure 7 was almost fixed to a specific longitude. There were no other stationary features observed beyond 10 Earth days because other features began to be observed in the evening region and immediately shifted to the night side, where UVI cannot observe.

All of the stationary features detected by UVI were also observed by LIR in the same geographical regions and at the same local time (Kouyama et al., 2017), although the stationary feature observed with LIR over eastern Aphrodite Terra (115–140°E) in mid-August of 2016 is not clearly seen in UVI data because it was near the evening side of the terminator. The almost one-to-one correspondence suggests a common dynamical mechanism, which is thought to be topographic gravity waves. However, since the extremely weak flow near the surface (Schubert et al., 1980) might not be strong enough to pass over the ridges, the mechanism for generating gravity waves needs further investigation. The tendency of stationary features to appear in local times ranging from noon to evening suggests a diurnal change in the atmospheric state, such as the static stability and the wind velocity, near the surface (Navarro et al., 2018).

Most of the images taken at the wavelength of 365 nm do not clearly show stationary features, as mentioned before. Among all the 365-nm images analyzed, stationary features are discernible only on 17 May 2016 (Figure 8). The difference in the appearance of stationary features between the two wavelengths implies a difference in the vertical distribution of the ultraviolet absorbers, as discussed in section 4.2.

3.2. Characteristics of Wavelike Structures

Here we estimate the amplitude and the horizontal wavelength of the wavelike structure seen in the 283-nm images taken on 17 May 2016 as a representative example. The spatial variation of the brightness along the solar incidence angle and emission angle was first removed by applying the Minnaert law (e.g., Lee et al.,

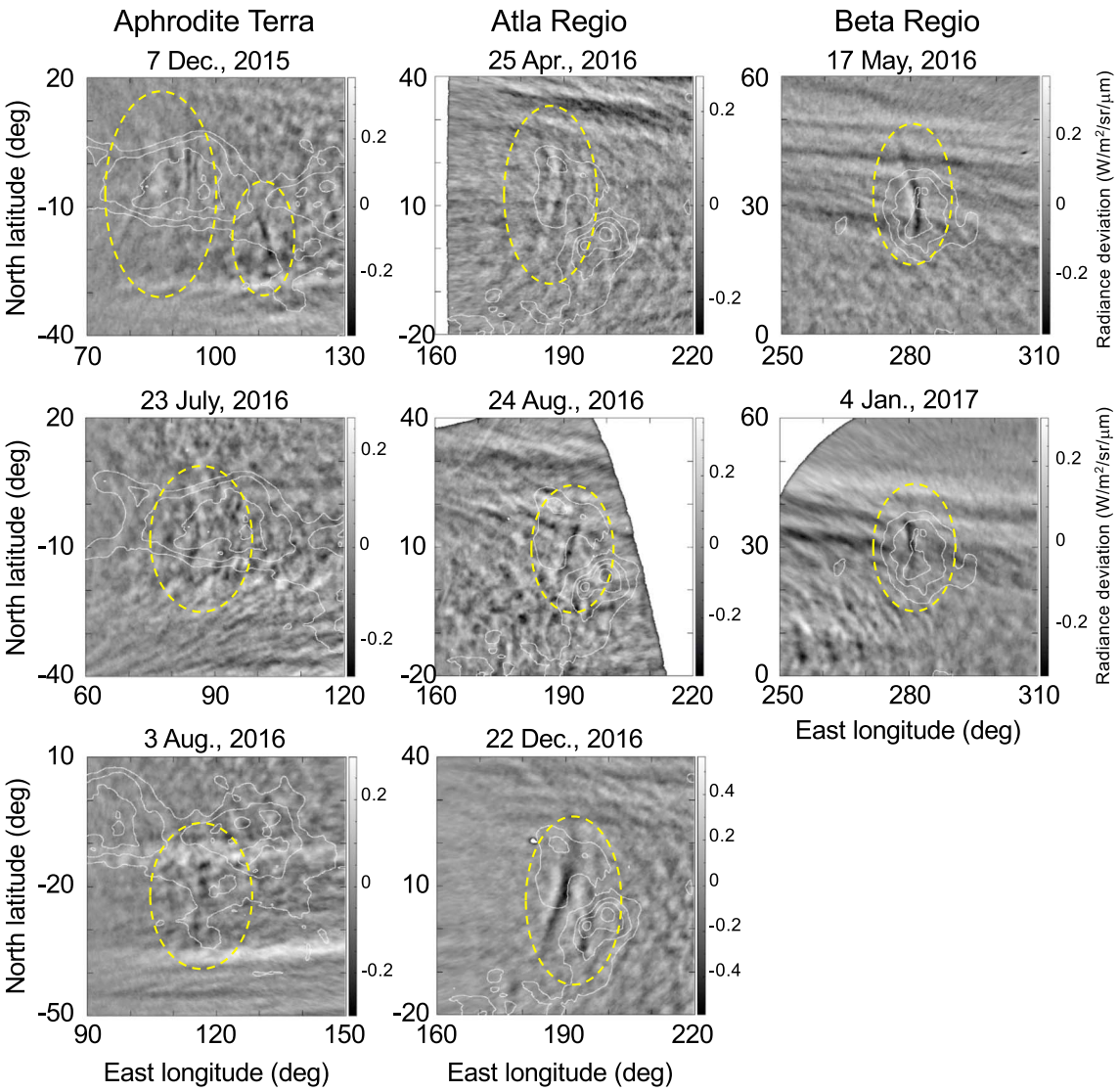

Figure 5. Stationary features observed in the 283-nm images from 7 December 2015 to 31 January 2017. Grayscale indicates the radiance ($W \cdot m^{-2} \cdot sr^{-1} \cdot \mu m^{-1}$) after averaging and high-pass filtering. The locations of the stationary features are indicated by ovals. White contours indicate altitudes with 1-km interval for altitudes higher than the global average corresponding to the radius of 6,052 km. The numbers of images averaged are given in the appendix.

2015) to obtain photometrically corrected images like the one shown in Figure 9. The Minnaert disk function is given by $(\cos i)^k (\cos e)^{k-1}$, where i is the incidence angle, e is the emergence angle, and k is an index that is determined by fitting the function to each image; $k = 1$ leads to the Lambert law.

Multiple images taken continuously were photometrically corrected and averaged to smooth out moving features, and then a zonal cross-section of the radiance near the center of a stationary feature was analyzed (Figure 10). A quadratic function was fitted to a longitudinal range of 20° centered at the stationary feature by a nonlinear least squares method, and then the fitted curve, which represents the background, was subtracted from the original cross-section to obtain the perturbation component. Finally, a sinusoidal function spanning one cycle was fitted to the perturbation associated with the stationary feature using a nonlinear least squares method to estimate the amplitude and the horizontal wavelength. High-pass filtering was not applied so that the waveform is not distorted. The relative amplitude of the radiance is obtained as ~1.2% and the wavelength as ~510 km. Given that the signal-to-noise ratio exceeds 100 (Yamazaki et al., 2018), the relative error after averaging seven images is <0.5%, and thus, an amplitude of this magnitude is detectable. The formal error estimate from the parameter covariance matrix is <10%; however, the quality of the fit is low, probably because various disturbances other than the stationary wave are superposed. The

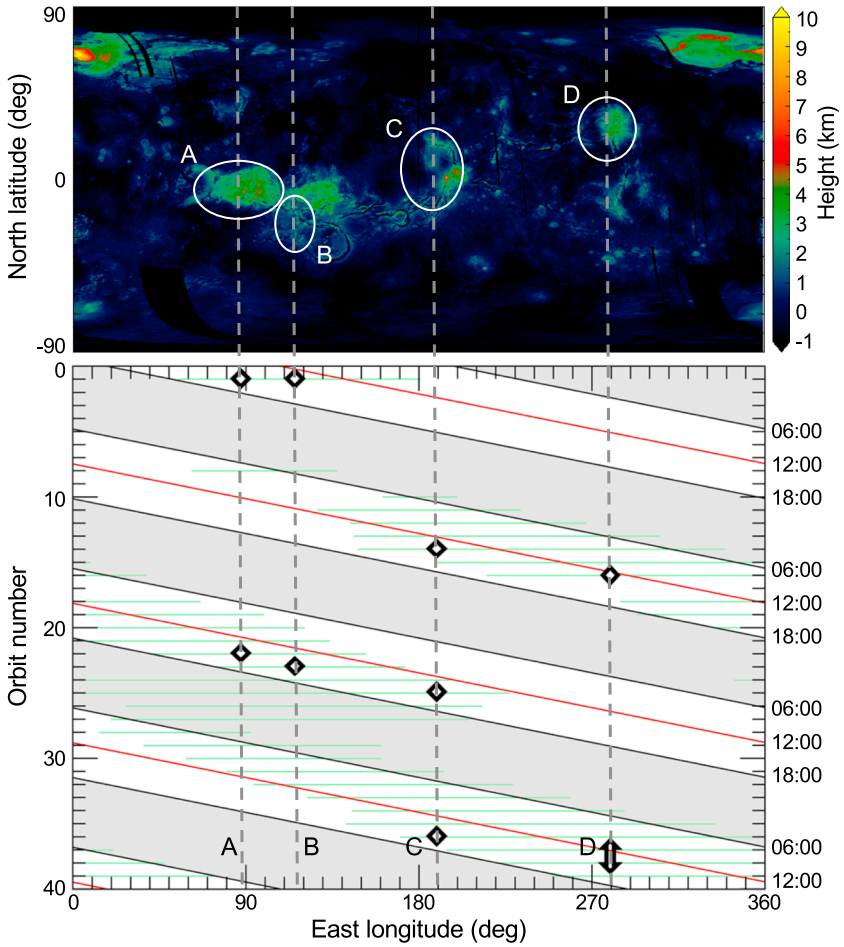

Figure 6. (Top) Locations where stationary features were observed in the 283-nm images, indicated by red circles on the topography map generated using Magellan altimetry data. The locations correspond to Aphrodite Terra (75–140°E), Atla Regio (180–210°E), and Beta Regio (270–300°E). (Bottom) The longitudinal span of UVI's field of view (green lines) and the local solar time (black and red lines) on the equator in each orbit. Symbols represent the longitude and the orbit where the stationary features were identified.

magnitude of the residual at the maximum and the minimum, which is ~40%, is taken as a measure of the uncertainties in the wave parameters.

The phase relationship between the stationary features seen in UVI 283 nm and LIR 10 μm images gives clues to the wave-induced transport of ultraviolet absorbers and cloud particles. For example, considering that SO_2 exists mostly below the cloud top in the basic state (Bertaux et al., 1996; Mahieux et al., 2015), the radiance in the SO_2 absorption band should decrease where SO_2 is carried upward relative to the cloud. The brightness temperature of the cloud top measured by LIR should decrease via adiabatic expansion in regions where the cloud is elevated.

Figures 11 and 12 show representative examples of pairs of UVI and LIR images showing stationary features and the zonal cross-sections across the structures. Photometric correction was applied to the UVI images, and then multiple images taken continuously were averaged for both UVI and LIR, while high-pass filtering was not applied. The amplitudes of the stationary features exceed the relative measurement errors of UVI and LIR before averaging, which are <1% and ~0.3 K, respectively; the measurement errors after averaging are even smaller. Roughly positive correlation is seen between the two wavelengths in the stationary structures, suggesting high (low) clouds in ultraviolet-dark (bright) regions. Most of the stationary features identified in this study show positive correlations between the two channels. Though vertical winds should transport both SO_2 and cloud particles, the observation suggests that the response is stronger for SO_2. The mechanism behind this is discussed in section 4.

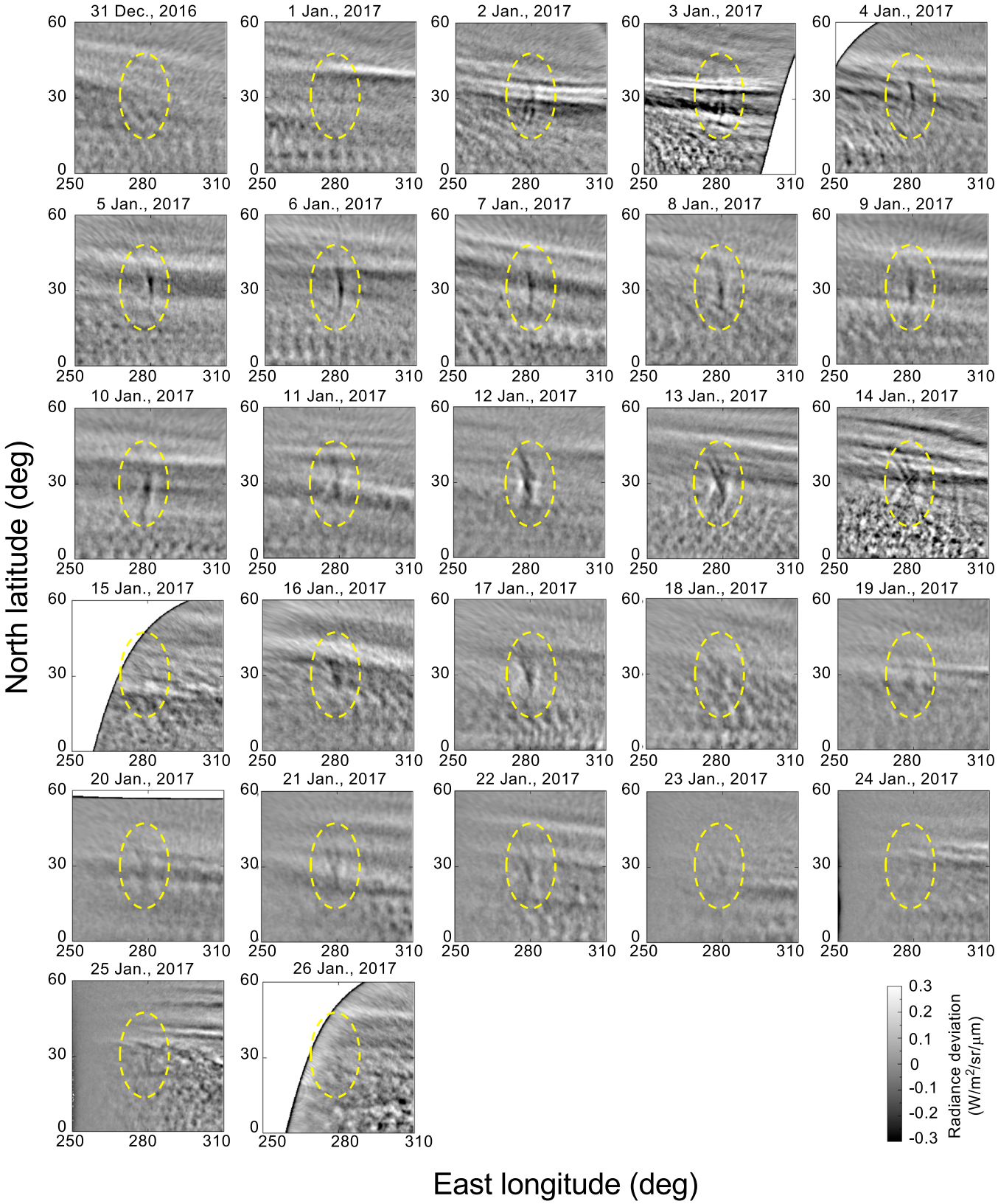

Figure 7. Temporal variation of the stationary feature near Beta Regio sampled every Earth day from 31 December 2016 (before appearance) to 26 January 2017 (out of the field of view). The location of the stationary feature is indicated by ovals. The local solar time changes monotonically from around 11:00 (31 December) to 16:20 (26 January). The spacecraft passed periapsis on 3, 14, and 26 January. The numbers of images averaged are given in the appendix.

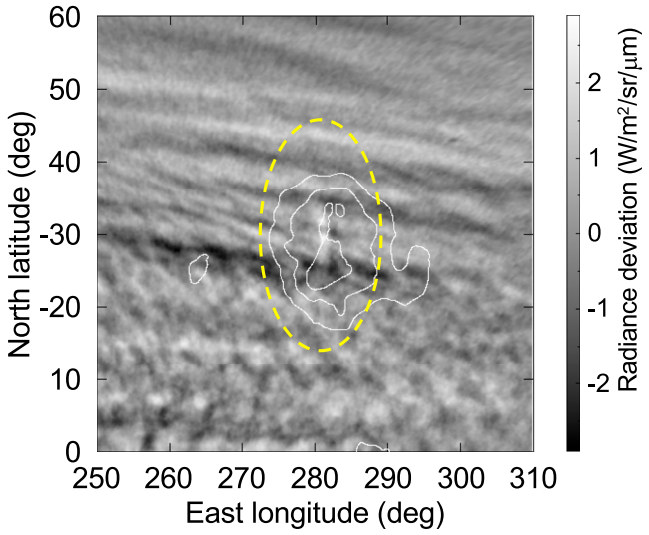

Figure 8. High-pass filtered map after averaging seven images at 365-nm wavelength taken on 17 May 2016 focusing on Beta Regio. The location of a stationary feature is indicated by an oval.

4. Response of the Cloud Top Atmosphere to a Gravity Wave

4.1. Model Description

The response of the atmosphere containing clouds and ultraviolet absorbers (such as SO_2) to a gravity wave is studied using a numerical model to understand the observed phase relationship (section 3.2). Focusing on the atmosphere near the cloud top where both the cloud particle number density and the ultraviolet absorber density decrease with height, the vertical distributions of those species are represented by their respective local scale heights. This approximation is expected to be appropriate for a narrow altitude range around the cloud top even though the vertical distributions in a broad altitude range do not obey the exponential law. Then, assuming a horizontally uniform atmosphere as the basic state, the vertical distribution of a minor species that represents cloud particles or the ultraviolet absorber is given by

$$\overline{n}_i(z) = n_{i0}\exp\left(-\frac{z-z_0}{H_i}\right), \tag{1}$$

where the subscript i represents cloud particles (i = cloud) or ultraviolet absorber (i = UV), $\overline{n}_i(z)$ is the basic number density before perturbation by the wave at the altitude z, n_{i0} is the number density at the reference altitude z_0 (=70 km), and H_i is the scale height of the minor species. The relative density perturbation of the minor species $n_i'/\overline{n}_i$ induced by a linear gravity wave in the absence of the Coriolis force is given by (Chiu & Ching, 1978)

$$\frac{n_i'}{\overline{n}_i} = -\frac{1}{\gamma-1}\left(1+\frac{\gamma H}{L_i}\right)\frac{N'}{\overline{N}}, \tag{2}$$

$$L_i \equiv \left[\frac{1}{\overline{n}_i}\frac{d\overline{n}_i}{dz}\right]^{-1} = -H_i, \tag{3}$$

$$\frac{N'}{\overline{N}} = A\ \exp\left[i\omega t - ikx - i\left(m+\frac{i}{2H}\right)z\right], \tag{4}$$

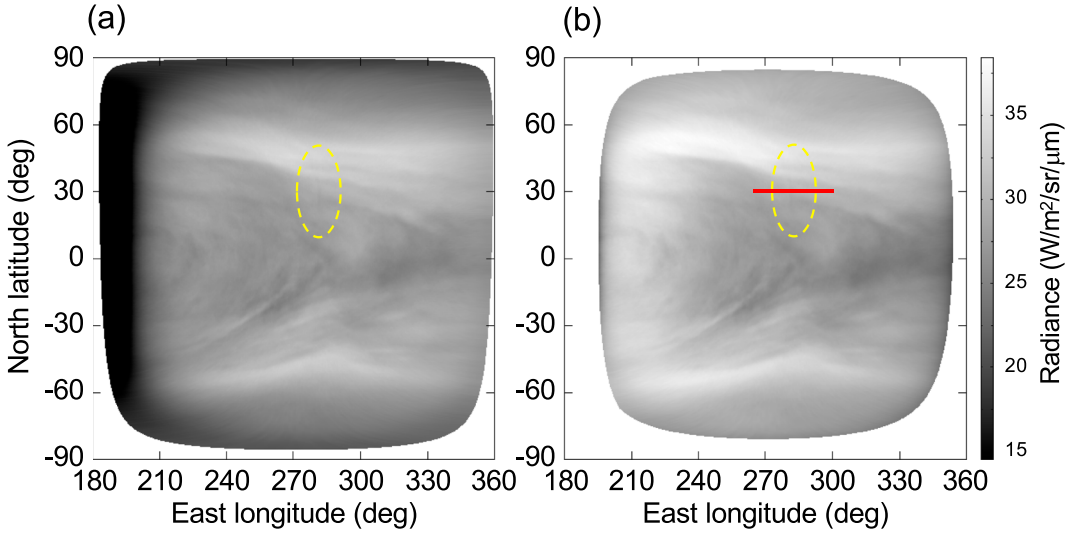

Figure 9. The 283-nm images acquired at 08:13 on 17 May 2016 (a) before and (b) after Minnaert photometric correction. Regions where the incidence angle or the emission angle exceeds 85° are not shown because of insufficient correction. The red line indicates the position where the zonal cross-section in Figure 10 was created. The locations of stationary features are indicated by ovals.

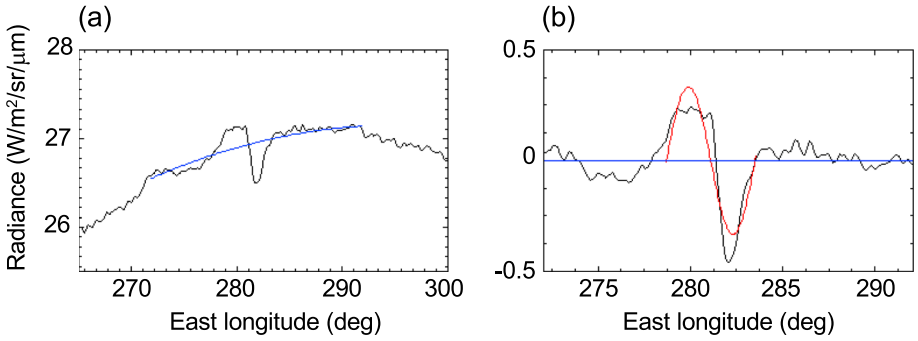

Figure 10. (a) Zonal cross-section of the radiance at 30°N across the bow-shaped structure observed on 17 May 2016 (Figure 9). Seven images were averaged. The black line is the observed radiance, and the blue line is a fitted quadratic function. (b) The residual radiance obtained by subtracting the fitted curve from the observed radiance. The red line indicates a sinusoidal function fitted to the stationary feature seen in the residual.

where $\gamma = 1.32$ is the ratio of specific heats at 70 km altitude for Venus' atmospheric composition (Seiff et al., 1985), H is the scale height of the background atmosphere, $N'/\overline{N}$ is the relative density variation of the background atmosphere associated with a gravity wave, A is the amplitude of the relative density variation, t is the time, x is the horizontal distance in the direction of wave propagation, ω is the intrinsic frequency, k is the horizontal wavenumber, and m is the vertical wavenumber. In this model, the minor species (clouds and ultraviolet absorbers) do not influence the propagation of the gravity wave, and the distributions of the minor species are disturbed mostly by vertical winds associated with the gravity wave. Since the wind field of the gravity wave is related to the atmospheric density fluctuation $N'/\overline{N}$, the density fluctuation of the minor species $n_i'/\overline{n}_i$ can be related to $N'/\overline{N}$ via equation (2). The contributions of chemical production and loss are ignored. The model above is based on the assumption that the background temperature is constant over the vertical extent of the layer structure and the intrinsic period of the wave is long compared to the Brunt-Väisälä frequency. The latter is satisfied as shown later.

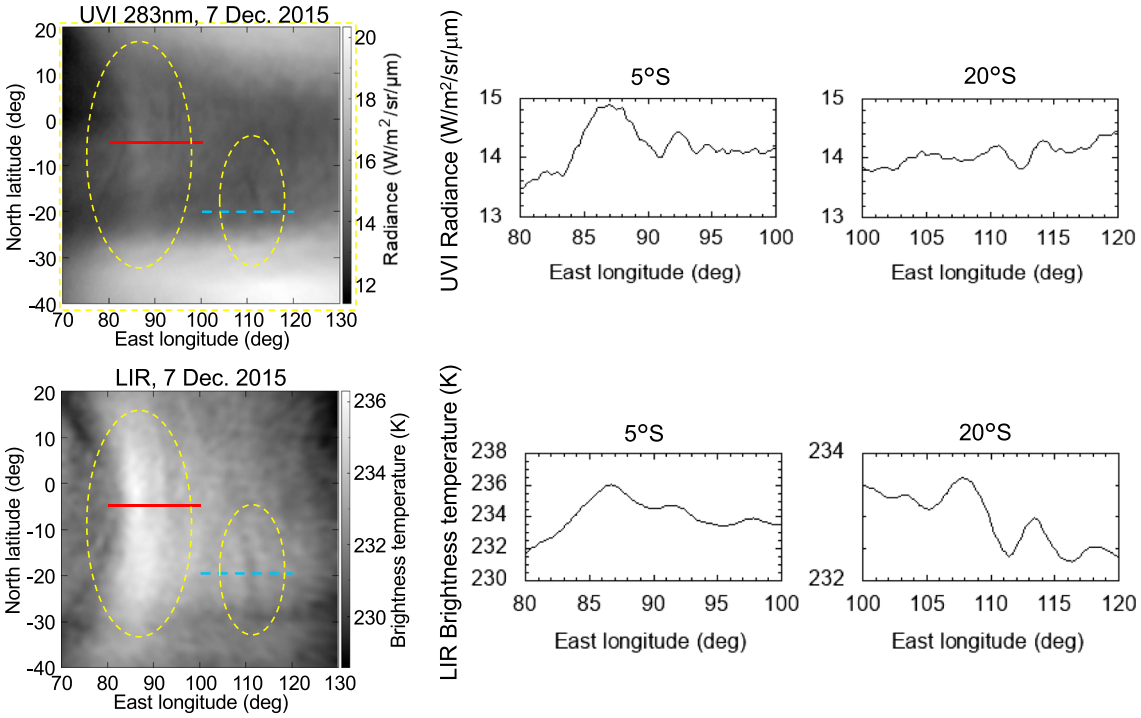

Figure 11. Stationary features observed in (upper left) Ultraviolet Imager (UVI) 283-nm image and (lower left) Longwave Infrared Camera (LIR) 10-μm image on 7 December 2015. Five images were averaged for UVI and 12 images for LIR. The zonal cross-sections along 5°S (red solid line) and 20°S (light blue dashed line) are shown on the right.

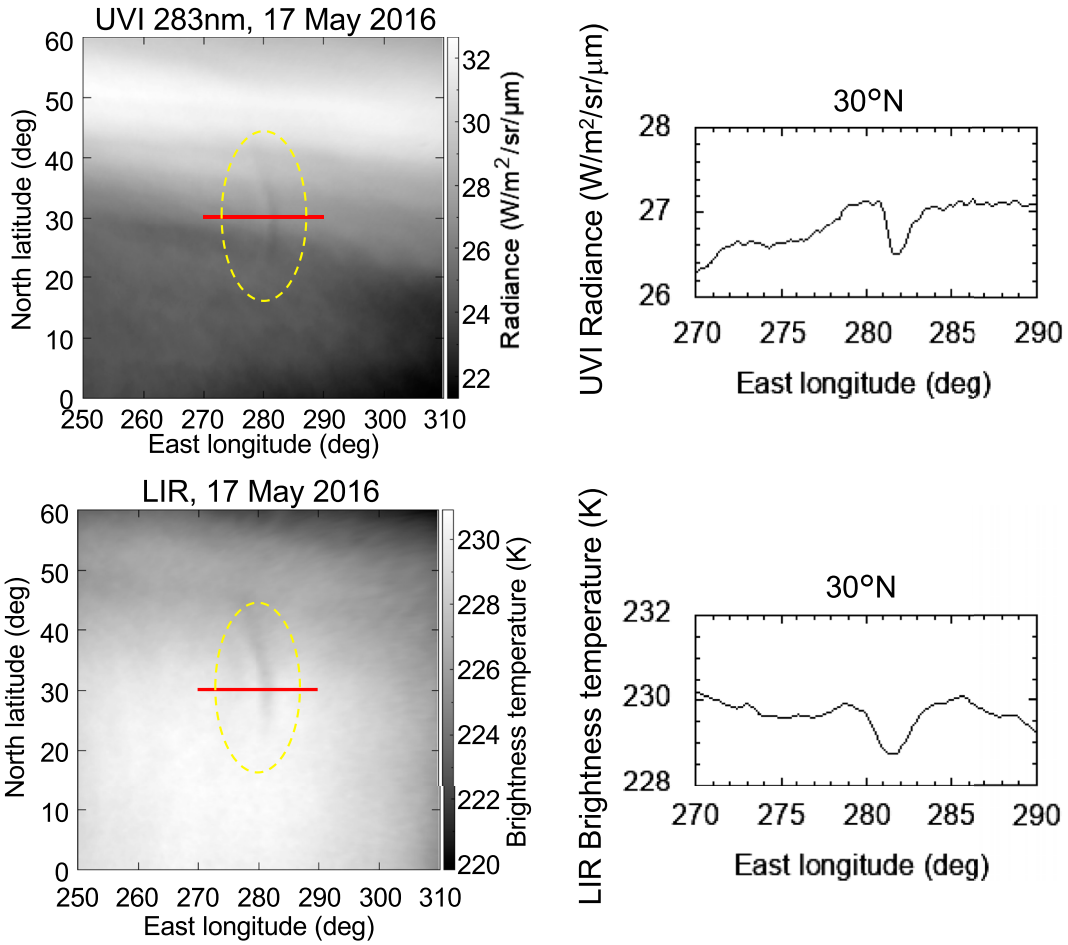

Figure 12. Stationary features observed in (upper left) Ultraviolet Imager (UVI) 283-nm image and (lower left) Longwave Infrared Camera (LIR) 10-μm image on 17 May 2016. Seven images were averaged for both UVI and LIR. The zonal cross-sections along 30°S (red solid line) are shown on the right.

The scattering of the solar ultraviolet radiation by the cloud is modeled with a single-scattering approximation (Kuznetsov et al., 2012). This approximation is valid for an optically thin atmosphere; a complete radiative transfer calculation including the effect of multiple scattering (e.g., Lee et al., 2017; Pérez-Hoyos et al., 2018), which is needed for Venusian clouds, is left for future studies. The relative reflectivity normalized by the reflectivity without the ultraviolet absorber for zero incidence and emission angles is given by

$$\alpha = \frac{\int_0^{z_{\rm top}} \sigma_{\rm cloud}\, n_{\rm cloud}(z)\, \exp\left[-2\int_z^{z_{\rm top}} \left(\sigma_{\rm cloud} n_{\rm cloud}(z') + \sigma_{\rm UV}\, n_{\rm UV}(z')\right) dz'\right] dz}{\int_0^{z_{\rm top}} \sigma_{\rm cloud}\, n_{\rm cloud}(z)\, \exp\left[-2\int_z^{z_{\rm top}} \sigma_{\rm cloud}\, n_{\rm cloud}(z') dz'\right] dz}, \tag{5}$$

where $n_{\rm cloud}$ and $n_{\rm UV}$ are the perturbed total densities ($n_i = \overline{n}_i + n_i'$), $\sigma_{\rm cloud}$ is the scattering cross-section of cloud particles, $\sigma_{\rm UV}$ is the absorption cross-section of the ultraviolet absorber, and $z_{\rm top}$ (=100 km) is the upper boundary of the model where $n_{\rm cloud}$ and $n_{\rm UV}$ are negligibly low. The numerator is proportional to the upward intensity with the source function replaced by one that ignores the scattering of the diffuse field but retains the scattering of the incident solar radiation (e.g., Chamberlain & Hunten, 1987; Kuznetsov et al., 2012). The $\sigma_{\rm cloud}\, n_{\rm cloud}(z)$ term that first appears in the integrand is the scattering cross-section of the clouds per unit volume at the altitude z where the radiation to be observed is scattered, the exponential term gives the attenuation along the incoming and outgoing paths, and the integration is performed from z to the top of the atmosphere. The denominator is the same as the numerator, but the attenuation by the ultraviolet absorber is not taken into account.

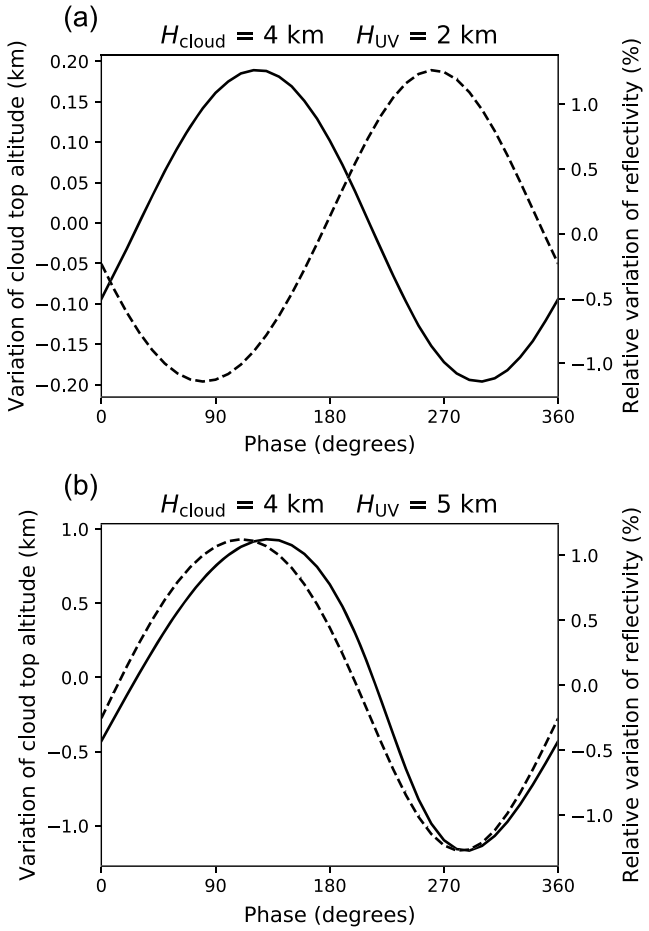

Figure 13. Examples of the variation of the cloud top altitude (solid) and the variation of the reflectivity relative to the basic value (dashed) along the phase of a gravity wave calculated by the model. The cloud scale height is 4 km, and the scale height of the ultraviolet absorber is (a) 2 km or (b) 5 km.

Using the model above, we can calculate the variations of the cloud top altitude and the ultraviolet reflectivity induced by a gravity wave as follows. The cloud top is defined as the altitude at which the contribution function peaks:

$$K(z) = \sigma_{\text{cloud}}\, n_{\text{cloud}}(z)\, \exp\left[-2\int_z^{z_{\text{top}}} \sigma_{\text{cloud}}\, n_{\text{cloud}}(z')dz'\right], \quad (6)$$

which is the integrand in the numerator of equation (5). Though the cloud top altitude at ~10-μm wavelength is expected to be 2–4 km lower than that in the ultraviolet (Ignatiev et al., 2009), the difference is ignored in this study.

Since the number density and the cross-section appear in equations (5) and (6) as a product $\sigma_i\, n_i$ (i = cloud or UV), the product $\sigma_i \overline{n}_i$ is given as a model parameter. $\sigma_{\text{cloud}}\overline{n}_{\text{cloud}}$ is determined so that the basic cloud top altitude is 70 km. $\sigma_{\text{UV}}\overline{n}_{\text{UV}}$ is determined so that the relative reflectivity α given by equation (5) in the basic state is ~0.8; this is a value typical for the ratio of the low-latitude brightness to the brightness in the bright polar band (Rossow et al., 1980), which is seen around 50°N in Figure 10. The phase relationship shown below does not depend on σ_{UV} as long as the ultraviolet absorber above the cloud top is optically thin, as is the case here.

The vertical distributions of the cloud and the ultraviolet absorber perturbed by the gravity wave at a certain phase ($\omega t - kx$) are calculated by using equations (1)–(4) and then substituted into equations (5) and (6) to obtain the reflectivity and the cloud top altitude. This procedure is repeated while changing the phase from 0 to 2π.

4.2. Results

We consider the stationary feature observed on 17 May 2016 (section 3.2). The parameters of the background atmosphere are taken from the values at 70-km altitude at latitudes <30° of Venus International Reference Atmosphere (Seiff et al., 1985): The temperature is 229.8 K, the gas constant used for calculating H is 191.3 J·K^{-1}·kg^{-1}, γ = 1.32, g = 8.67 m/s^2, T_0 = 229.8 K, and the Brunt-Väisälä frequency is N_B= 0.018 s^{-1}. Though newer data are available (Limaye et al., 2017), the difference from Venus International Reference Atmosphere is small around the cloud top (65–70 km) at low latitudes according to radio occultations (Imamura et al., 2017; Tellmann et al., 2009); we confirmed that the difference hardly changes the results below. The scale height is calculated to be H ~ 5.1 km. The zonal wind speed at the cloud top is assumed to be 100 m/s (e.g., Horinouchi et al., 2018), meaning that the intrinsic phase velocity is also 100 m/s in the opposite direction. From these parameters and the observed horizontal wavelength of ~510 km (section 3.2), the wave period is 1.4 hr, corresponding to ω ~ 0.0012 s^{-1}. Using the dispersion relation for gravity waves in the absence of background shear and the Coriolis force (Fritts & Alexander, 2003)

$$\omega = \frac{N_B k}{\sqrt{k^2 + m^2 + 1/4H^2}}, \quad (7)$$

m is calculated to be ~0.15 km^{-1}, corresponding to a vertical wavelength of ~42 km.

The cloud scale height is assumed to be H_{cloud}= 4 km based on the values at low latitudes retrieved from the combination of Visible and InfraRed Thermal Imaging Spectrometer (VIRTIS) and radio occultation measurements on Venus Express by Lee et al. (2012). The estimate of the SO_2 scale height ranges from 1 to 5 km in the previous observations (Esposito et al., 1979; Mahieux et al., 2015; Na et al., 1994). To demonstrate the dependence on the scale height, we show results for H_{UV} = 2 km as an intermediate value and H_{UV} = 5 km as the upper limit; these are shorter or longer than the cloud scale height of H_{cloud}=4 km. By adjusting the atmospheric density amplitude A of the gravity wave so that the observed reflectivity amplitude of 1.2% relative to the background (section 3.2) is reproduced, the amplitude is estimated to be A = 2%

when $H_{UV} = 2$ km and $A = 11\%$ when $H_{UV} = 5$ km. Note, however, that this is considered as an order-of-magnitude estimate because of the large uncertainty in the amplitude of the reflectivity and the simplified radiation modeling.

Figure 13 shows the variation of the cloud top altitude and the reflectivity along the wave's phase. The oscillations of the cloud top altitude and the reflectivity are almost opposite in phase for $H_{UV} = 2$ km, while they are in phase for $H_{UV} = 5$ km. Generally, they are opposite in phase for $H_{cloud} > H_{UV}$ and in phase for $H_{cloud} < H_{UV}$. This result is explained by equations (2) and (3): The relative density fluctuation of the minor species $n_i'/\overline{n}_i$ becomes larger for a larger vertical gradient of the mixing ratio, that is, a smaller scale height of the species. When $H_{cloud} > H_{UV}$, the relative variation of the absorber density exceeds that of the cloud, and thus, the column amount of the absorber above the cloud top increases (decreases) at phases where the cloud top is elevated (lowered). Conversely, when $H_{cloud} < H_{UV}$, the relative variation of the cloud density exceeds that of the absorber, and thus, the column amount of the absorber above the cloud top decreases (increases) at phases where the cloud top is elevated (lowered). The observed positive correlation between the 283-nm brightness and the brightness temperature at the stationary features means that high (low) clouds occurs in low (high) reflectivity regions, suggesting that the SO_2 scale height is shorter than the cloud scale height near the cloud top.

The model also implies that the variation of the column density of any ultraviolet absorber above the cloud top would vanish when the scale heights of the absorber and the cloud are equal because the densities of the absorber and the cloud would change equally. This might explain the observed tendency that stationary features are not clearly seen at the wavelength of 365 nm: The scale height of the "unknown absorber" might be close to the cloud scale height.

5. Summary and Discussion

We investigated the characteristics of stationary features seen in the ultraviolet images taken by UVI on board Akatsuki. In order to extract stationary features buried in the background pattern, we averaged multiple images and applied high-pass filtering. As a result, eight events were identified in the 283-nm (SO_2 absorption band) images obtained in the period from 7 December 2015 to 31 January 2017. They show bow-shaped structures extending in the north-south direction with a zonal scale of 300–500 km and a meridional scale of 2,000–3,000 km. The stationary features appear only above highlands, suggesting that they are manifestations of topographic gravity waves and tend to appear in the local time region from noon to evening. They are synchronized with the stationary features detected in the cloud top temperature images taken by LIR (Fukuhara, Futaguchi, et al., 2017; Kouyama et al., 2017). No stationary feature was observed above Maxwell Mons, which is the highest mountainous area on Venus.

Comparison of the stationary features between UVI 283 nm and LIR brightness temperature images shows that the SO_2 absorption and the cloud top height tend to have positive correlation. To understand this relationship, we constructed a simple advection model for the response to a gravity wave. The result suggests that the observed positive correlation requires a SO_2 scale height smaller than the cloud scale height near the cloud top. This might be attributed to the photochemical loss of SO_2 and the production of sulfuric acid droplets near the cloud top. On the other hand, at 365 nm (absorption by unknown absorbers), stationary features are unclear compared to at 283 nm, suggesting that the scale height of the unknown absorber is close to the cloud scale height.

As for nonstationary features, prominent albedo contrasts exist also at 365 nm (Rossow et al., 1980; Titov et al., 2012; Sánchez-Lavega et al., 2016), and albedo marks are similar between 283 and 365 nm (Limaye et al., 2018). The reason for the difference between stationary and nonstationary features at 365 nm is unclear. A possible cause is the short time scale of the dynamics related to the stationary features; given the horizontal wavelength of ~400 km and the intrinsic phase speed of ~100 m/s, the intrinsic period of the gravity wave is ~1 hr. Longer time scale processes may involve photochemistry as well as dynamics. Detailed investigation on this issue is left for future studies.

The momentum transport by topographic gravity waves potentially has a large influence on the momentum balance of the upper atmosphere. If the gravity waves are not saturated, radiative damping and molecular viscosity are considered as major processes attenuating the waves. Based on a theoretical estimation of the radiation relaxation time, which exceeds one Earth day up to 90-km altitude for a vertical wavelength of

30 km (Crisp, 1989), the effect of radiative damping is small for topographic waves having intrinsic periods of hours at cloud heights. At higher altitudes the propagation characteristics should depend on the local time because of the local time-dependence of the background zonal wind (e.g., Alexander, 1992). The waves should reach thermospheric heights and decay via molecular viscosity on the dusk side where the westward superrotation extends to the thermosphere, while the waves will decay via radiative damping or critical layer absorption on the dawn side where the superrotation vanishes at high altitudes. Characterization of topographic gravity waves in a broad altitude region is crucial for understanding the momentum deposition by those waves and the resultant deceleration of the superrotation above the cloud. Note, however, that waves with vertical wavelengths of tens of kilometers (section 4.2) cannot be detected by radio occultation measurements, which focus on vertical wavelengths shorter than several kilometers (e.g., Imamura et al., 2018; Tellmann et al., 2012).

Further studies of topographic gravity waves are needed for understanding the dynamical state of the surface boundary layer where they originate. It would be possible to constrain the static stability and the wind speed near the surface based on the wave parameters at the cloud top (Fukuhara, Futaguchi, et al., 2017; Navarro et al., 2018). Such information is important for elucidating the exchange of angular momentum between the atmosphere and the solid planet that eventually leads to the maintenance of the superrotation.

Appendix A

The numbers of images averaged in producing the figures are listed in Table A1. Each date indicates a time slot from around 06:00 on that day to around 06:00 on the next day.

Table A1
Numbers of Images Averaged in Producing the Figures

Date	Figure	Number of images
7 December 2015	1, 2, 3, 4, 5, 11	5
25 April 2016	5	6
17 May 2016	5, 8, 9, 10, 12	7
23 July 2016	5	6
3 August 2016	5	8
24 August 2016	5	3
22 December 2016	5	5
31 December 2016	7	8
1 January 2017	7	8
2 January 2017	7	8
3 January 2017	7	6
4 January 2017	5, 7	10
5 January 2017	7	8
6 January 2017	7	8
7 January 2017	7	7
8 January 2017	7	8
9 January 2017	7	8
10 January 2017	7	11
11 January 2017	7	10
12 January 2017	7	10
13 January 2017	7	10
14 January 2017	7	5
15 January 2017	7	9
16 January 2017	7	8
17 January 2017	7	8
18 January 2017	7	8
19 January 2017	7	8
20 January 2017	7	9
21 January 2017	7	8
22 January 2017	7	8
23 January 2017	7	10
24 January 2017	7	10
25 January 2017	7	6
26 January 2017	7	6

Acknowledgments

We acknowledge the Akatsuki project team for supporting the observations. The data used are available at JAXA's data archive (https://darts.jaxa.jp/planet/project/akatsuki). The two anonymous reviewers provided valuable comments.

References

Alexander, M. J. (1992). A mechanism for the Venus thermospheric superrotation. *Geophysical Research Letters*, *19*(22), 2207–2210. https://doi.org/10.1029/92GL02110

Bertaux, J.-L., Khatuntsev, I. V., Hauchecorne, A., Markiewicz, W. J., Marcq, E., Lebonnois, S., et al. (2016). Influence of Venus topography on the zonal wind and UV albedo at cloud top level: The role of stationary gravity waves. *Journal of Geophysical Research: Planets*, *121*, 1087–1101. https://doi.org/10.1002/2015JE004958

Bertaux, J.-L., Widemann, T., Hauchecorne, A., Moroz, V. I., & Ekonomov, A. P. (1996). VEGA 1 and VEGA 2 entry probes: An investigation of local UV absorption (220–400 nm) in the atmo- sphere of Venus (SO_2, aerosols, cloud structure). *Journal of Geophysical Research*, *101*(E5), 12,709–12,745. https://doi.org/10.1029/96JE00466

Blamont, J. E., Young, R. E., Seiff, A., Ragent, B., Sagdeev, R., Linkin, V. M., et al. (1986). Implications of the VEGA balloon results for Venus atmospheric dynamics. *Science*, *231*(4744), 1422–1425. https://doi.org/10.1126/science.231.4744.1422

Chamberlain, J. W., & Hunten, D. M. (1987). *Theory of planetary atmospheres*. San Diego, CA: Academic Press.

Chiu, Y. T., & Ching, B. K. (1978). The response of atmospheric and lower ionospheric layer structures to gravity waves. *Geophysical Research Letters*, *5*(6), 539–542. https://doi.org/10.1029/GL005i006p00539

Crisp, D. (1989). Radiative forcing of the Venus mesosphere. II—Thermal fluxes, cooling rates, and radiative equilibrium temperatures. *Icarus*, *77*(2), 391–413. https://doi.org/10.1016/0019-1035(89)90096-1

Esposito, L. W. (1980). Ultraviolet contrasts and the absorbers near the Venus cloud tops. *Journal of Geophysical Research*, *85*(A13), 8151–8157. https://doi.org/10.1029/JA085iA13p08151

Esposito, L. W., Winick, J. R., & Stewart, A. I. (1979). Sulfur dioxide in the Venus atmosphere: Distribution and implications. *Geophysical Research Letters*, *6*(7), 601–604. https://doi.org/10.1029/GL006i007p00601

Fritts, D. C., & Alexander, M. J. (2003). Gravity wave dynamics and effects in the middle atmosphere. *Reviews of Geophysics*, *41*(1), 1003. https://doi.org/10.1029/2001RG000106

Fukuhara, T., Futaguchi, M., Hashimoto, G. L., Horinouchi, T., Imamura, T., Iwagaimi, N., et al. (2017). Large stationary gravity wave in the atmosphere of Venus. *Nature Geoscience*, *10*(2), 85–88. https://doi.org/10.1038/ngeo2873

Fukuhara, T., Taguchi, M., Imamura, T., Hayashitani, A., Yamada, T., Futaguchi, M., et al. (2017). Absolute calibration of brightness temperature of the Venus disk observed by the Longwave Infrared Camera onboard Akatsuki. *Earth, Planets and Space*, *69*(1), 141. https://doi.org/10.1186/s40623-017-0727-y

Fukuhara, T., Taguchi, M., Imamura, T., Nakamura, M., Ueno, M., Suzuki, M., et al. (2011). LIR: Longwave infrared camera onboard the Venus Orbiter Akatsuki. *Earth, Planets and Space*, *63*(9), 1009–1018. https://doi.org/10.5047/eps.2011.06.019

Horinouchi, T., Kouyama, T., Lee, Y. J., Murakami, S., Ogohara, K., Takagi, M., et al. (2018). Mean winds at the cloud top of Venus obtained from two-wavelength UV imaging by Akatsuki. *Earth, Planets and Space*, *70*(1), 10. https://doi.org/10.1186/s40623-017-0775-3

Ignatiev, N. I., Titov, D. V., Piccioni, G., Drossart, P., Markiewicz, W. J., Cottini, V., et al. (2009). Altimetry of the Venus cloud tops from the Venus Express observations. *Journal of Geophysical Research*, *114*, E00B43. https://doi.org/10.1029/2008JE003320

Imamura, T., Ando, H., Tellmann, S., Pätzold, M., Häusler, B., Yamazaki, A., et al. (2017). Initial performance of the radio occultation experiment in the Venus orbiter mission Akatsuki. *Earth, Planets and Space*, *69*(1), 137. https://doi.org/10.1186/s40623-017-0722-3

Imamura, T., Miyamoto, M., Ando, H., Häusler, B., Pätzold, M., Tellmann, S., et al. (2018). Fine vertical structures at the cloud heights of Venus revealed by radio holographic analysis of Venus Express and Akatsuki radio occultation data. *Journal of Geophysical Research: Planets*, *123*(8), 2151–2161. https://doi.org/10.1029/2018JE005627

Kouyama, T., Imamura, T., Taguchi, M., Fukuhara, T., Sato, T. M., Yamazaki, A., et al. (2017). Topographical and local time dependence of large stationary gravity waves observed at the cloud top of Venus. *Geophysical Research Letters*, *44*, 12,098–12,105. https://doi.org/10.1002/2017GL075792

Kuznetsov, A., Melnikova, I., Pozdnyakov, D., Seroukhova, O., & Vasilyev, A. (2012). Calculating radiative characteristics with the single scattering approximation. In *Remote Sensing of the Environment and Radiation Transfer* (Chap. 14, pp. 139–146). Berlin, Heidelberg: Springer. https://doi.org/10.1007/978-3-642-14899-6_14

Lee, Y. J., Imamura, T., Schroder, S. E., & Marcq, E. (2015). Long-term variations of the UV contrast on Venus observed by the Venus Monitoring Camera on board Venus Express. *Icarus*, *253*, 1–15. https://doi.org/10.1016/j.icarus.2015.02.015

Lee, Y. J., Titov, D. V., Tellmann, S., Piccialli, A., Ignatiev, N., Pätzold, M., et al. (2012). Vertical structure of the Venus cloud top from the VeRa and VIRTIS observations onboard Venus Express. *Icarus*, *217*(2), 599–609. https://doi.org/10.1016/j.icarus.2011.07.001

Lee, Y. J., Yamazaki, A., Imamura, T., Yamada, M., Watanabe, S., Sato, T. M., et al. (2017). Scattering properties of the Venusian clouds observed by the UV Imager on board Akatsuki. *Astronomy Journal*, *154*(2), 44. https://doi.org/10.3847/1538-3881/aa78a5

Limaye, S. S., Lebonnois, S., Mahieux, A., Pätzold, M., Bougher, S., Bruinsma, S., et al. (2017). The thermal structure of the venus atmosphere: Intercomparison of Venus Express and ground based observations of vertical temperature and density profiles. *Icarus*, *294*, 124–155. https://doi.org/10.1016/j.icarus.2017.04.020

Limaye, S. S., Watanabe, S., Yamazaki, A., Yamada, M., Satoh, T., Sato, T. M., et al. (2018). Venus looks different from day to night across wavelengths: Morphology from Akatsuki multispectral images. *Earth, Planets and Space*, *70*(1). https://doi.org/10.1186/s40623-018-0789-5

Mahieux, A., Vandaele, A. C., Robert, S., Wilquet, V., Drummond, R., Chamberlain, S., et al. (2015). Venus mesospheric sulfur dioxide measurement retrieved from SOIR on board Venus Express. *Planetary and Space Science*, *113*, 193–204. https://doi.org/10.1029/2008JE003143

Mills, F. P., Esposito, L. W., & Yung, Y. L. (2007). Atmospheric composition, chemistry, and clouds. In L. W. Esposito, E. R. Stofan, & T. E. Cravens (Eds.), *Exploring Venus as a terrestrial planet*, (pp. 73–100). Washington, DC: American Geophysical Union. https://doi.org/10.1029/176GM06

Na, C. Y., Esposito, L. W., McClintock, W. E., & Barth, C. A. (1994). Sulfur dioxide in the atmosphere of Venus. 2: Modeling results. *Icarus*, *112*(2), 389–395. https://doi.org/10.1006/icar.1994.1193

Nakamura, M., Imamura, T., Ishii, N., Abe, T., Kawakatsu, Y., Hirose, C., et al. (2016). AKATSUKI returns to Venus. *Earth, Planets and Space*, *68*(1), 75. https://doi.org/10.1186/s40623-016-0457-6

Navarro, T., Schubert, G., & Lebonnois, S. (2018). Atmospheric mountain wave generation on Venus and its influence on the solid planet's rotation rate. *Nature Geoscience*, *11*(7), 487–491. https://doi.org/10.1038/s41561-018-0157-x

Ogohara, K., Takagi, M., Murakami, S., Horinouchi, T., Yamada, M., Kouyama, T., et al. (2017). Overview of Akatsuki data products: Definition of data levels, method and accuracy of geometric correction. *Earth, Planets and Space*, *69*(1), 167. https://doi.org/10.1186/s40623-017-0749-5

Peralta, J., Hueso, R., Sánchez-Lavega, A., Lee, Y. J., Muñoz, A. G., Kouyama, T., et al. (2017). Stationary waves and slowly moving features in the night upper clouds of Venus. *Nature Astronomy*, *1*(8), 187. https://doi.org/10.1038/s41550-017-0187

Pérez-Hoyos, S., Sánchez-Lavega, A., García-Muñoz, A., Irwin, P. G. J., Peralta, J., Holsclaw, G., et al. (2018). Venus upper clouds and the UV absorber from MESSENGER/MASCS observations. *Journal of Geophysical Research: Planets*, *123*(1), 145–162. https://doi.org/10.1002/2017JE005406

Piccialli, A., Titov, D. V., Sanchez-Lavega, A., Peralta, J., Shalygina, O., Markiewicz, W. J., & Svedhem, H. (2014). High latitude gravity waves at the Venus cloud tops as observed by the Venus Monitoring Camera on board Venus Express. *Icarus*, *227*, 94–111. https://doi.org/10.1016/j.icarus.2013.09.012

Rossow, B. W., Genio, D. D. A., Limaye, S. S., & Travis, D. L. (1980). Cloud morphology and motions from Pioneer Venus images. *Journal of Geophysical Research*, *85*(A13), 8107–8128. https://doi.org/10.1029/JA085iA13p08107

Sánchez-Lavega, A., Lebonnois, S., Imamura, T., Read, P., & Luz, D. (2017). The atmospheric dynamics of Venus. *Space Science Reviews*, *212*(3-4), 1541–1616. https://doi.org/10.1007/s11214-017-0389-x

Sánchez-Lavega, A., Peralta, J., Gomez-Forrellad, J. M., Hueso, R., Pérez-Hoyos, S., Mendikoa, I., et al. (2016). Venus cloud morphology and motions from ground-based images at the time of the Akatsuki orbit insertion. *The Astrophysical Journal*, *833*(1), L7. https://doi.org/10.3847/2041-8205/833/1/L7

Schubert, G., Covey, C., Del Genio, A., Elson, L. S., Keating, G., Seiff, A., et al. (1980). Structure and circulation of the Venus atmosphere. *Journal of Geophysical Research*, *85*(A13), 8007–8025. https://doi.org/10.1029/JA085iA13p08007

Seiff, A., Schofield, J. T., Kliore, A. J., Taylor, F. W., & Limaye, S. S. (1985). Models of the structure of the atmosphere of Venus from the surface to 100 kilometers altitude. *Advances in Space Research*, *5*(11), 3–58. https://doi.org/10.1016/0273-1177(85)90197-8

Tellmann, S., Häusler, B., Hinson, D. P., Tyler, G. L., Andert, T. P., Bird, M. K., et al. (2012). Small-scale temperature fluctuations seen by the VeRa Radio Science Experiment on Venus Express. *Icarus*, *221*(2), 471–480. https://doi.org/10.1016/j.icarus.2012.08.023

Tellmann, S., Pätzold, M., Häusler, B., Bird, M. K., & Tyler, G. L. (2009). Structure of the Venus neutral atmosphere as observed by the Radio Science experiment VeRa on Venus Express. *Journal of Geophysical Research*, *114*, E00B36. https://doi.org/10.1029/2008JE003204

Titov, D. V., Markiewicz, W. J., Ignatiev, N. I., Song, L., Limaye, S. S., Sanchez-Lavega, A., et al. (2012). Morphology of the cloud tops as observed by the Venus Express Monitoring Camera. *Icarus*, *217*(2), 682–701. https://doi.org/10.1016/j.icarus.2011.06.020

Vandaele, A. C., Korablev, O., Belyaev, D., Chamberlain, S., Evdokimova, D., Encrenaz, T., et al. (2017). Sulfur dioxide in the Venus atmosphere: I. Vertical distribution and variability. *Icarus*, *295*, 16–33. https://doi.org/10.1016/j.icarus.2017.05.003

Yamazaki, A., Yamada, M., Lee, Y. J., Watanabe, S., Horinouchi, T., Murakami, S., et al. (2018). Ultraviolet Imager on Venus orbiter Akatsuki and its initial results. *Earth, Planets and Space*, *70*(1), 23. https://doi.org/10.1186/s40623-017-0772-6